The M5 Cell: A Color-Opponent Intrinsically Photosensitive Retinal Ganglion Cell

Maureen E. Stabio[*,1,5], **Shai Sabbah**[2,6], **Lauren Quattrochi**[2,6], **Marissa C. Ilardi**[2], **P. Michelle Fogerson**[2], **Megan Leyrer**[2], **Jordan M. Renna**[3], **Min Tae Kim**[2], **Inkyu Kim**[2], **Matthew Schiel**[4], **Kevin L. Briggman**[4], and **David M. Berson**[2]

[1]Department of Cell & Developmental Biology, University of Colorado School of Medicine, Aurora, CO 80018, USA

[2]Department of Neuroscience, Brown University, Providence, RI 02912, USA

[3]Department of Biology, University of Akron, OH 44325, USA

[4]Circuit dynamics and Connectivity Unit, National Institute of Neurological Disorders and Stroke, Bethesda, MD, 20892, USA

Summary

Intrinsically photosensitive retinal ganglion cells (ipRGCs) combine directly photosensitivivity through melanopsin with synaptically-mediated drive from classical photoreceptors through bipolar-cell input. Here, we sought to provide a fuller description of the least understood ipRGC type, the M5 cell, and discovered a distinctive functional characteristic — chromatic opponency (ultraviolet excitatory, green inhibitory). Serial electron microscopic reconstructions revealed that M5 cells receive selective UV-opsin drive from Type 9 cone bipolar cells, but also mixed cone signals from bipolar Types 6, 7 and 8. Recordings suggest that both excitation and inhibition are driven by the ON channel, and that chromatic opponency results from M-cone-driven surround inhibition mediated by wide-field spiking GABAergic amacrine cells. We show that M5 cells send axons to the dLGN, and are thus positioned to provide chromatic signals to visual cortex. These findings underscore that melanopsin's influence extends beyond unconscious reflex functions to encompass cortical vision, perhaps including the perception of color.

[*]Corresponding Author: Maureen Estevez Stabio, PhD, University of Colorado School of Medicine, Department of Cell & Developmental Biology, Mail Stop F435, 13001 E 17th Place, Aurora, CO 80045, USA, 303-724-7461, maureen.stabio@ucdenver.edu.
[5]Lead Contact
[6]These authors contributed equally

Introduction

Intrinsically photosensitive retinal ganglion cells (ipRGCs) differ from other retinal output neurons because their light responses are driven not only by synaptic signals derived from classical rod and cone photoreceptors but also by autonomous phototransduction, mediated by the photopigment melanopsin. They are diverse, and are now thought to comprise five types, M1 through M5 cells (Schmidt et al., 2011; Sonoda and Schmidt, 2016). Relatively little is known about the M5 type (Dhande and Huberman, 2014; Ecker et al., 2010; Estevez et al., 2012; Schmidt et al., 2014; Schmidt et al., 2011; Schmidt and Kofuji, 2009, 2011; Zhao et al., 2014). Though described as a highly-branched ON stratifying ipRGC subtype, the M5 cell's morphology has yet to be quantitatively distinguished from that of other ON monostratified ipRGCs. M5 cells have much weaker melanopsin-based photoresponses than the original M1 ipRGC type and stronger antagonism from the receptive-field surround (Ecker et al., 2010; Zhao et al., 2014). These observations suggest that M5 cells, like M4 (ON alpha) cells, may contribute to 'image-forming' or spatial vision, whereas M1 cells serve non-image-forming visual reflex circuits, including those for circadian and pupillary control.

Here, we combine patch recording, intracellular staining, retrograde and viral labeling, and serial blockface electron microscopic reconstruction to provide a much fuller account of the structure and function of the M5 ipRGC type. The most striking functional feature of these cells is their pronounced chromatic opponency. They have sustained ON responses, receptive-field centers driven by balanced input from UV and mid-wavelength cone (M-cone) opsins, and a strong suppressive surround dominated by input from M-cones. This spectral opponency is unique among all ipRGC subtypes; M1–M4 cells lack it. We show by serial EM reconstruction that the UV ON-center mechanism derives in part from direct input from UV-selective Type-9 cone bipolar cells. Electrophysiological and pharmacological studies show that the M-cone dominant surround derives from wide-field GABAergic amacrine cells acting at least in part at the axon terminals of afferent bipolar cells. We show that spectrally opponent M5 cells contribute axons to the visual thalamus and may thus provide chromatic signal to primary visual cortex of mice, and contribute to their capacity for color vision (Denman et al., 2017; Jacobs et al., 2004; Rhim et al., 2017).

Results

M5 cells are morphologically unique among ipRGCs

We dye-filled M5 cells along with other EGFP-positive ipRGCs in Opn4$^{Cre/+}$;Z/EG$^{+/-}$ mice during patch recording (n = 17) or by targeted injection with sharp micropipettes (n = 27). M5 cells were morphologically distinct from other known ipRGC types (M1 – M4). Their dendrites were monostratified in the ON sublamina of the inner plexiform layer (IPL; Fig. 1A), whereas M1 and M3 cells deployed dendrites at least partly in the OFF sublamina. Though M2 and M4 ipRGCs also have monostratified dendritic arbors in the inner ON sublayer of the IPL, M5 cells were distinguishable from them on other grounds. M5 cells generally had more compact and highly branched dendritic profiles than M2 and M4 cells (mean field diameter: 224 ± 44 μm; mean total branch points: 52.1 ± 12.5; n = 44; Fig. 1 and Table 1). Soma diameter of M5 cells averaged 14.2 ± 2.4 μm (n = 44, Fig. 1 and Table 1);

their somas were smaller and typically more spherical than M4 somata and their dendrites stratified slightly closer to the ganglion-cell layer. M5 cells differed significantly from other monostratified ipRGCs in soma diameter, dendritic-field diameter, and total number of dendritic branch points (p<0.01; Table 1). M5 cells also differed from M4 cells (but not M2 cells) in total dendritic length and number of primary dendrites (Table 1). The difference in stratification was particularly helpful in distinguishing M5 from M4 cells in the temporal retina, where M4 cells are most densely distributed and have reduced dendritic field diameters (Bleckert et al., 2014).

We were able to partially reconstruct the mosaic of M5 cells from confocal stacks of GFP fluorescence in Opn4$^{Cre/+}$;Z/EG$^{+/-}$ retinas, optimized for visualizing GFP-tagged dendrites (Fig. 1C–E). In such material, most labeled RGCs could be recognized as belonging to one of the known types of ipRGCs, based on soma size and dendritic branching pattern and stratification (Fig. 1C–E). We used this strategy to identify and reconstruct the dendritic arbors of presumed M5 cells (and other ipRGC types) in several such confocal stacks (~250×250 μm). The dendritic profiles shown in Fig. 1 D–E are certainly incomplete; we truncated the tracing wherever we could no longer confidently determine which of two closely overlapping processes belonged to the traced cell. Despite incomplete reconstruction, the arbors of neighboring M5 cells consistently overlapped (Fig. 1D), indicating that M5 cells tile the retina with a coverage greater than unity.

M5 cells have weak intrinsic responses and low levels of melanopsin expression

We confirmed two earlier reports (Ecker et al., 2010; Zhao et al., 2014) that M5 cells are intrinsically photosensitive (Fig. 2A). Under glutamatergic and ionotropic inhibitory synaptic blockade, bright, full-field light steps (480 nm) evoked in every M5 cell a slow depolarization and inward current (−10.3 ± 1.6 pA, n = 10). These intrinsic responses were smaller than those of M2 and M4 cells recorded under the same experimental conditions (M2: −16.3 ± 2.7 pA, $n = 8$; M4: −22.0 ± 3.8 pA, $n = 21$, Estevez et al., 2012), confirming an earlier report (Zhao et al., 2014) that M5 cells have the weakest melanopsin responses of all known ipRGC types. The intrinsic melanopsin response (~10 pA) in M5 cells is at least an order of magnitude smaller than the extrinsic, synaptically mediated response (100–400 pA, Figs. 2B, 3B). Thus, rod/cone-driven synaptic signals dominate over melanopsin in shaping the light response of M5 cells.

Consistent with their weak intrinsic response, M5 cells were only marginally immunoreactive for melanopsin. Using an antibody protocol that readily marks M1–M3 ipRGCs, including their fine dendritic processes, only a minority of M5 cells exhibited unequivocal melanopsin immunolabeling. With tyramide signal amplification (Fig. 2A), however, the majority of dye-filled M5 cells tested (10/14) exhibited clear melanopsin immunofluorescence. The remaining cells either had equivocal labeling (2/14), or lacked detectable labeling altogether (2/14). Immunolabeling was invariably limited to the perisomatic region of M5 cells; their dendrites were never clearly labeled.

Chromatic opponency of synaptically-driven light responses in M5 cells

The synaptically-driven light responses of M5 cells were chromatically opponent. To full-field ultraviolet (UV; 360nm) illumination, M5 cells exhibited sustained ON responses, consisting of a maintained depolarization and spiking in current-clamp recordings (Fig. 2B, top left trace), and a continuous inward current under voltage clamp at -64 mV as in Estevez et al, 2012 (Fig. 2B, bottom left traces). These synaptically mediated responses were typically much larger than melanopsin-driven responses and had much faster onset and termination kinetics. However, they shared the sustained quality of the intrinsic response, lasting throughout a 10 second light step (Fig. 2B, left bottom trace), the longest duration we tested. In contrast, a full-field green stimulus (520 nm) was suppressive. In current clamp, it suppressed spiking and slightly hyperpolarized the cell (Fig. 2B, top right trace), while in voltage clamp it induced an outward current (Fig. 2B, bottom right traces) which was sustained for at least 10 sec (Fig. 2B, right bottom trace). Termination of a full-field green stimulus did not evoke an excitatory OFF response. Such chromatic opponency is absent in other ipRGC types (Estevez et al., 2012; Schmidt and Kofuji, 2010; Weng et al., 2013), and data not shown).

It has been reported that some otherwise chromatically unselective mouse RGCs can exhibit chromatic tuning in the opsin transition zone, due to topographic gradients in expression of the two cone opsins (Chang et al., 2013). This cannot fully account for the chromatic opponency of M5 cells, because we observed it both ventral and dorsal to the opsin transition zone.

Chromatic opponency of M5 cells exhibits center-surround spatial organization

To dissect the spatial organization of this chromatic coding, compared the cells' responses to narrow-band spectral stimuli delivered only to the receptive-field center (165 μm diameter spot) or to both the center and surround (620 μm diameter spot). The large spots evoked the same sort of response as had full-field stimuli: excitatory inward current for UV stimuli and an inhibitory outward current for green ones (Fig. 3A). However, this spectral opponency was lost when stimulating with a small spot, which evoked strong inward currents for both wavelengths (Fig. 3A). This chromatic opponency was observed in M5 cells even when the melanopsin gene was knocked out (Opn4$^{cre/cre}$;Z/EG$^{+/-}$ mice; n = 2; data not shown), indicating that intrinsic phototransduction in M5 cells is not required for their chromatic opponency.

Surround antagonism could be evoked by stimuli of both wavelengths; that is, large spots typically evoked smaller responses than small ones. However, the magnitude of this surround antagonism depended on wavelength. For the UV stimulus, it was quite variable among cells (Fig. 3A, B, G, H, Q) and overall the difference in current amplitude between small and large UV spots was not statistically significant [$d = -166.4$, (CI: -334.51, 195.94), p = 0.485]. For green stimuli, however, surround antagonism was strong enough to invert the net evoked current from inward to outward (Fig. 3A, B, G, H), and this difference was statistically significant [$d = -230.7$ (CI: -387.1, 109.4), p < 0.001]. To summarize the effect of spot size, we used the ratio of light-evoked excitatory currents evoked by large spots to that evoked by small spots (Fig. 3Q). Ratios <1 indicate surround antagonism while those >1

indicate surround facilitation. This ratio was variable for UV spots (0.85 ± 0.57; mean $\pm$ SD) with individual ratio values falling either below or above 1. In contrast, despite showing similar variation (-0.36 ± 0.59; mean $\pm$ SD), the ratio for green spots was negative, indicating an antagonistic surround, for virtually all cells tested, with only a single exception (Fig. 3Q).

Stimuli evoking strong surround antagonism reduced membrane current noise (Fig. 2B, right middle and Fig. 3A, right). To quantify this effect, we plotted the standard deviation (SD) of the current during the plateau of the light response relative to its pre-stimulus baseline (Fig. 3B, inset, n = 8). Current noise was reduced by large mid-wavelength spots (520 nm, mean SD = -2.0 ± 0.9 pA), but was increased by other light stimuli, including small spots of the same wavelength (520 nm, mean SD = 4.1 ± 1.4 pA) and spots of shorter wavelength, whether large (360 nm, mean SD = 4.8 ± 1.3 pA) or small (360 nm, mean SD = 7.6 ± 2.7 pA). M5 cells, like M4 cells, had somewhat higher current noise at rest than other ipRGCs (mean SD of current in dark for 2 s pre-stimulus = 13.1 ± 5.4 pA; n = 8 M5 cells).

The ON-center mechanism of M5 cells receives blended opsin inputs

We generated a simple model to estimate the relative contribution of the two cone opsin pigments to the receptive-field center of M5 cells. Rods were omitted from the model because they were severely bleached under our recording conditions (see Estevez et al., 2012) and presumably contributed little to the observed responses. Pure M-opsin drive failed to account for the spectral behavior of M5 receptive-field centers because it predicted a response to green light (520 nm) ~2 log units higher than observed (Fig. S1A). A model with pure UV cone opsin input also failed, predicting sensitivity to monochromatic green light (520 nm) far lower than we observed (Fig. S1B). An optimal fit was obtained when we blended inputs from the two opsins at virtually equal strength (51% UV opsin input, 49% M-opsin input; Fig. S1C). These data suggest that bipolar inputs to M5 cells, in the aggregate, carry both cone-opsin pigment signals although the response to small UV spots was generally larger than that of small green spots.

All M5 cell input is driven by the ON channel and opponency is GABA-mediated

To assess the synaptic mechanism of the chromatic opponency we introduced pharmacological antagonists into the bath. These experiments were conducted in two distinct cell samples, so separate pre-drug control data are shown for each. In the first series, we applied a cocktail of ionotropic GABA-receptor blockers: ((1, 2, 5, 6-Tetrahydropyridin-4-yl)methylphosphinic acid (TPMPA) for $GABA_C$ and gabazine for $GABA_A$). This inverted the sign of the response induced by large green spots, from inhibitory outward to excitatory inward current (Fig. 3E, F, $n = 4$). Responses to small and large green spots no longer differed significantly [d = -2.5 (CI: -346.8, 389.4), p = 0.926] as they did in the pre-drug control [d = -255.2, (CI: -439.3, -101.9), p < 0.001]. For UV stimuli, the drugs also eliminated the apparent preference for small spots over large ones (Fig. 3D, F), although that preference was not statistically significant [control: d = 166.3 (CI: -433.6, 50.8), p = 0.158; during drug application: d = 25.2, (CI: -205.6, 298.7), p = 0.504].

Unlike the pronounced effects of blocking GABA receptors, blocking glycinergic transmission with strychnine had little effect on chromatic opponency. Under strychnine, the response to large green spots remained a net outward current (Fig. 3I, J; n = 5) and was statistically smaller than the response to small green spots [d = −169.4 (CI: −354.4, −70.3), p < 0.001] just as in the pre-drug control [d = −176.2, (CI: −508.9, −61.7), p < 0.001]. For UV stimuli, large spots did not evoke statistically smaller responses than small spots in control solution ([d = 42.4 (CI: −371.4, 337.2), p = 0.375], and this did not change in the presence of strychnine [d = −14.2, (CI: −300.8, 308.8), p = 0.906].

Blocking sodium spikes with tetrodotoxin (TTX, an antagonist of voltage-gated Na$^+$ channels) also suppressed surround antagonism. It inverted the response to large green spots and abolished the surround antagonism (Fig. 3K, L; n = 5), just as blocking GABAergic transmission had done (Fig. 3E, F). Under spike blockade, responses to small and large green spots were statistically indistinguishable [d = 6.2 (CI: −261.0, 95.5), p = 0.897] as were responses to small and large UV spots [d = 32.2, (CI: −444.7, 692.3), p = 0.861]. Together, these experiments demonstrate that the surround antagonism in M5 cells is shaped by GABAergic transmission dependent on spiking activity, likely in polyaxonal amacrine cells.

To test whether pH-sensitive feedback from horizontal cells onto photoreceptors plays a role in the chromatic opponency, we supplemented the bath with the HEPES buffer (4-(2-hydroxyethyl)-1-piperazineethanesulfonic acid; (Cadetti and Thoreson, 2006; Thoreson et al., 2008). This inverted the response to a large green spot from a small net outward to a small net inward current (Figure 3M, N, *n* = 6; compare with Fig. 3G, H). Surround attenuation remained larger for green than for UV stimuli, but this difference no longer reached statistical significance [*d* = −66.3 (CI: −318.7, 13.3), p = 0.121]. Responses to small and large UV spots, did not differ significantly either [*d* = −62.5, (CI: −347.7, 405.3), p = 0.723], but this was true even under control conditions (Fig. 3H). Overall, though suppressing horizontal cell feedback may have subtly affected the surround, it did not abolish the preference of M5 cells for extended UV stimuli over extended green ones.

Lastly, applying L-AP4, which blocks the ON pathway by interfering with neurotransmission between photoreceptors and ON bipolar cells, completely eliminated all synaptically-driven responses to light, regardless of spatial extent or wavelength (Fig. 3O, P; *n* = 6). Responses to small and large green spots [d = 0.7 (CI: −11.9, 5.7), p = 0.779] as well as responses to small and large UV spots [d = 1.0, (CI: −15.5, 13.5), p = 0.594] did not differ significantly.

To facilitate comparisons among these pharmacological experiments, we plot in Figure 3R the ratio of maximum light-evoked currents evoked by large spots versus small ones, first for green and then for UV stimuli (Figs. 3E, I, K, and M), under each pharmacological manipulation. Under control conditions, surround antagonism was strong for green stimuli (ratio <<1), whereas it was generally weak for UV stimuli (ratio near 1). Gabazine and TTX strongly attenuated the suppressive green surround effect (Fig. 3R, right panel), HEPES less so, and strychnine not at all. For UV stimuli, where the surround was weak to begin with,

the drugs generally had very little effect, though gabazine again appeared to eliminate the modest surround suppression seen in the control bath.

Serial electron microscopic analysis indicates a diversity of bipolar inputs to M5 cells

We used serial blockface electron microscopy (SBEM) to identify ribbon synaptic inputs to M5 cells and to reconstruct the presynaptic bipolar cells that provided them. We used the adult mouse SBEM volume of Ding et al. (Ding et al., 2016), which extends from the ganglion cell layer through the full IPL. We first traced all somata of the ganglion-cell layer (n=259), then reconstructed the dendritic profiles of all of those that were large enough to be plausible RGCs (n = 113). Reconstructions, though mostly incomplete, were detailed enough to distinguish monostratified cells from bistratified ones and to determine the primary depth of dendritic stratification. Among these, only two were plausible M5 cells, combining somata of intermediate size with a monostratified, moderately highly branched dendritic arbor in the inner ON sublayer of the IPL. These two cells (#7180 and #7027) were fully reconstructed (Fig. 4, A and B, respectively). Their dendritic arbors stratified exclusively in the inner half of the ON sublayer, below the ON cholinergic bands, whose laminar position we inferred by partial reconstruction of 8 presumed ON-OFF direction-selective ganglion cells (Fig. 4D). Dendritic branch points occurred at about the same spatial density in these two RGCs ($929/mm^2$ and $1479/mm^2$) as in our chromatically-opponent patch-recorded M5 cells (1358 ± 595 branch points/mm^2; mean $\pm$ SD; n = 17). Although soma diameters of 18.9 and 19.0 μm were somewhat larger than the mean diameter of 14.2 um (Table 1) we measured by light microscopy, they were within the range (10 – 19 μm) we observed, thought this comparison is of questionable value given differential shrinkage associated with the two methods.

We mapped ribbon synaptic contacts onto these two presumed M5 cells (Fig. 4A and B; Movie File S1). and then reconstructed 27 of the presynaptic bipolar cells providing these contacts. All were ON cone bipolar cells; none were rod bipolar cells. All cone bipolar cell types with axonal arbors in the inner ON sublamina were represented among presynaptic cell sample. Type 6 cells were common, and easily recognizable from their compact axon terminal fields and the presence of ribbons and small side branches just distal to the ON ChAT band (Fig. 4E, G). Type 7 bipolar cells had slightly larger arbors and narrowly stratified terminals at the proximal margin of the ON ChAT band (Fig. 4E, G). The remaining bipolar cells had larger, more sparsely branched axonal arbors (Fig. 4F) and stratified closer to the ganglion cell layer than did Type 7 cells. These appeared to comprise a mixture of Type 8 and Type 9 bipolar cells. In accord with an earlier study (Helmstaedter et al., 2013), Type 9 bipolar cells in our sample had larger, more sparsely branched arbors than Type 8 cells, and the two types appeared to form independent mosaics of terminal fields (Fig. 4F). We encountered several examples in which a single bipolar cell independently contacted both M5 cells at different ribbon synapses.

All ribbon contacts onto M5 dendrites appeared to be dyad synapses. This was not always obvious in single-planes views (see Fig. 5J, L), but was invariably confirmed by serial EM analysis., The postsynaptic profile paired with the M5 dendrite was almost always an amacrine cell, as expected from current understanding of dyad ribbon contacts in the IPL.

However, in a few cases the other postsynaptic process lacked any discernable vesicles for at least 20 μm in either direction, suggesting that it (like its paired M5 process) was an RGC dendrite. Indeed, in one such case, serial reconstruction showed that both postsynaptic processes were M5-cell dendrites, one each from cells #7180 and #7027 (Fig. 5E). We observed a similar arrangement for a Type 9 ON cone bipolar terminal (Fig. 5K), although in that case the second presumptive M5 dendrite belonged to neither #7180 or #7027, but to a third cell that we were able to reconstruct only partially, because its soma lay outside the volume (Fig. 4C, blue arbor). The stratification and branching pattern of this ganglion cell were consistent with M5-cell morphology (Fig. 4C and D). These three presumptive M5-cell dendritic arbors overlapped extensively, consistent with the M5 mosaic reconstructed from Cre-dependent labeling of melanopsin-expressing ganglion cells (Fig. 1D).

Regarding the more typical postsynaptic partners at ribbon contacts onto M5 cells — the amacrine processes — some of these contained synaptic vesicles right at the dyad synapse (e.g. Fig. 5A, C, and H). Others lacked vesicles locally, but exhibited vesicle-packed varicosities dozens of microns away. Thus, there is ultrastructural evidence for both feedforward excitation of medium-to-wide-field amacrine cells and for feedback inhibition of the bipolar terminal at the cone-bipolar-to-M5 ribbon synapse.

We crosschecked these findings by mining the connectomic database of neuronal types in mouse retina generated and shared by Helmstaedter et al. (2013). Using the same morphological criteria as for our own analysis, we identified three presumptive M5 cells in this data set (cells #33, 35 and 36, Table S1), comprising most of the ganglion cells included within Type 12 by Helmstaedter et al. (2013). They included a fourth cell (#34) within their Type 12, but we excluded it because it was weakly bistratified, with a minor arbor in the OFF sublayer, as we confirmed by inspection of the original image data. We never encountered such bistratification among M5 cells.

Because synaptic specializations such as ribbons were not visible in their material, Helmstaedter et al. (2013) inferred synaptic connections between cells from the amount of contact between their plasma membranes, with contact areas >1 μm^2 estimated to have a $>95\%$ probability of being an actual synapse. Supplemental data these authors provided on contact area between all reconstructed cells was broadly consistent with our findings. All of the cone bipolar cell types found to be presynaptic to M5 cells in our analysis (Types 6, 7, 8, and 9; Fig. 7) met the criterion for such connectivity in the volume of Helmstaedter and colleagues (Table S1). Significantly, Type 9 cells were much more likely to be connected to the presumed M5 cells than to any other ganglion cell type. In fact, about 75% of all contact between Type 9 bipolar cells and RGC dendrites were traced to Type 12 ganglion cells (i.e., presumptive M5 cells). Similarly, Type 12 (M5) cells appeared to receive a particularly large fraction (~15%) of their total bipolar contact from Type 9 cells, whereas no other RGC type received even 1% of its bipolar input from Type 9 cells. However, some caution is warranted; their surface-contact analysis also implied that nearly a quarter of the bipolar input to Type 12 (M5) RGCs derives from rod bipolar cells, but we never saw such contacts in our analysis despite mapping hundreds of ribbon inputs.

M5 cells project to the dLGN

Might M5 cells contribute to geniculo-cortical color vision? Originally, ipRGCs were thought to almost entirely lack projections to the dorsal lateral geniculate nucleus (dLGN) (Hattar et al., 2006). However, a more sensitive Cre-based reporter that marks M5 cells along with all other known ipRGC types does label substantial numbers of retinogeniculate afferents (Ecker et al., 2010), at least some of which derive from M4 ipRGCs (ON alpha cells, Estevez et al., 2012). To determine whether M5 cells might also contribute, we injected a retrograde tracer into the dLGN and characterized the morphology of retrolabeled ipRGCs (Fig. 6). In all cases, histology confirmed that the injection site involved the dLGN, but not the intergeniculate leaflet (IGL), ventral lateral geniculate nucleus (vLGN), or optic tract. We also confirmed that the retrograde labeling was topographically restricted as expected from dLGN retinotopy (Pfeiffenberger et al., 2006).

We used two approaches in these studies. In one (Fig. 6A–C), we injected the retrograde tracer CTB-594 into the dLGN of melanopsin-reporter mice (Opn4$^{Cre/+}$;Z/EG$^{+/−}$), then targeted fluorescent double-labeled ipRGCs in the contralateral eye for intracellular dye filling *in vitro*. These studies yielded three examples of dye-filled retrolabeled cells that clearly matched the morphology of M5 cells (Fig. 6C). In a second approach (Fig. 6D–L), we injected the dLGN of Opn4$^{Cre/+}$ mice with red fluorescent latex microspheres ('beads'), a retrograde tracer that diffuses less, and is relatively ineffective in labeling passing axons compared to CTB. Morphology of ipRGCs was revealed in these experiments by intraocular injection of a Cre-dependent AAV2 virus that induces GFP expression in infected Cre-expressing cells. Though the high density of GFP labeled processes precluded full reconstruction of individual ipRGCs, we could nonetheless easily identify M1, M2 and M4 subtypes of ipRGCs based on soma size, branching architecture and stratification (Fig. 6H, I). We also identified many presumptive M5 cells, based on their relatively small cell bodies, fine dendrites, and moderately highly branched, monostratified arbors in the inner ON sublayer of the IPL (Fig. 6G). A few of these incompletely reconstructed cells could arguably have been grouped with either M2 or M5 cells, but otherwise subtype identification was unambiguous. The arbors of presumptive M5 cells overlapped considerably, confirming earlier evidence that they comprise a retinal mosaic (Fig. 1D). In general, about half of the presumptive M5 cells were retrolabeled in the zone of densest retrolabeling. Similar results were obtained in five separate experiments of this type.

Discussion

M5 cells are true ipRGCs; we have confirmed their intrinsic photosensitivity and detected their expression of melanopsin protein. We provide the first comprehensive evidence for the distinctness of the M5 ganglion-cell type within the heterogeneous class of ganglion-cell photoreceptors. M5-cell dendritic arbors are more compact and highly branched than those of the M1–M4 types. Previously characterized ganglion-cell types that may correspond to M5 cells include the Type 12 cell of Helmstaedter et al. (2013), the G6 cell of Völgyi et al. (2009), G28 of Baden et al. (2016) and the U cell of Sümbül et al. (2014). Morphological criteria alone are generally sufficient to distinguish M5 cells from other ipRGCs (M1–M4). Within the limited parameter space we have explored here, there is modest overlap between

M5 cells and two other monostratified ON ipRGC subtypes (the M2 and M4 cells), but in most cases distinguishing them is straightforward. Still, the uniqueness of the M5 type among ipRGCs is most strikingly evident in the functional domain: only M5 cells exhibit marked, consistent chromatic opponency.

Circuitry for chromatic opponency: the center mechanism

Through electrophysiology and ultrastructural analysis, we have sketched the outlines of circuitry underlying the spatial and spectral opponency M5-cell receptive fields (Fig. 7). The center mechanism receives a blend of UV-opsin and M-opsin excitation, and this is consistent with known circuitry. There are two cone ypes in mice. By far the more abundant type expresses a mixture of M-opsin and UV-opsin, but the mixture shifts from almost exclusive M-opsin expression dorsally to almost exclusive UV-opsin expression ventrally. The second type, the rarer 'true' short-wavelength cone, expresses only UV opsin regardless of retinal location. We observed abundant ribbon inputs to M5 cells from all four ON cone bipolar types deploying their axonal arbors within the inner ON IPL, amongst the M5-cell dendrites (i.e., Types 6, 7, 8 and 9). Three of these types (6, 7, and 8) receive non-selective cone input in the outer retina (Wässle et al., 2009), and thus carry a topographically varying blend of the two opsin signals. The remaining bipolar input, from Type 9 cone bipolar cells, appears to carry a pure UV opsin signal because their dendrites selectively contact true UV cones.

The strength of the UV-opsin drive to M5 ipRGCs may be special to them. A connectomic surface-contact analysis (Helmstaedter et al., 2013) provides evidence for disproportionate Type 9 UV-cone-selective bipolar input onto presumptive M5 cells (Results and Table S1). By contrast, another monostratified ON ipRGC — the M4 cell or ON-alpha cell — is reported to receive bipolar input predominantly from Type 6 cone bipolar cells (Schwartz et al., 2012). In M5 cells, UV stimuli restricted to the receptive-field center generally evoked larger responses than flux-matched green stimuli, but spectral modeling indicates that contributions from the two cone opsins are roughly of equal strength.

Though rods presumably also contribute to the center, we could not evaluate their contribution under our experimental conditions. Our ultrastructural analysis suggests that M5 cells lack direct input from rod bipolar ribbon synapses, as is generally assumed for mammalian ganglion cells (but see Helmstaedter et al., 2013). Scotopic responses of M5 cells are likely mediated, as for other ON RGCs (including other ipRGCs), through some combination of rod-bipolar-AII amacrine (primary) pathway and rod-cone coupling (secondary rod pathway).

Surround mechanisms

The surround appears dominated by M-opsin signals and is strong enough when engaged to invert the ON-center response to green stimuli. UV opsin appears to contribute to the surround in some cells, but not all. Such variability could be linked to the retinal location of recorded cells; M-cones surely contribute to the surround, but will carry more or less UV opsin signal based on location. Even true UV cones could make some contribution to the surround which, like the center, is mediated by the ON channel (Fig. 3O); all ON cone

bipolar cells apparently receive some synaptic input from true UV cones ((Behrens et al., 2016)). However, the dominance of M-opsin over UV-opsin drive to the antagonistic surround suggests that the responsible amacrine-cell network is weighted against UV-opsin, as it would be, for example, if it lacked any contribution from Type 9 (UV-selective) bipolar cells (Fig. 7). The longer-wavelength preference of the surround could be further enhanced if UV-opsin, through true UV cones and Type 9 bipolar cells, actively suppressed the surround-generating circuit. Among mouse bipolar cells, only Type 1 OFF bipolar cells make selective contacts with M-cones (Behrens et al., 2016). Sign-inverted signals from these bipolar cells seem excluded as a source of the M-dominant surround because the surround is apparently driven solely by the ON-channel (Fig. 3O).

The surround inhibition seems likely to be mediated mainly by medium to wide-field spiking ON GABAergic amacrine cells. It is abolished by blockade of ionotropic GABAergic inhibition (Fig. 3E, F), of the ON channel (Fig. 3O, P), or of voltage-gated sodium channels (Fig. 3K). This amacrine-cell circuit appears to act at least partly by inhibiting the bipolar terminals that drive the M5's center mechanism because surround stimulation reduces current noise in M5 cells and triggers a net outward current, presumably by suppressing a resting glutamatergic inward current (Fig. 3A, B). Thus, the surround apparently acts presynaptically to suppress bipolar drive to the M5 cell's center mechanism. Our ultrastructural findings make this arrangement plausible; vesicle-containing amacrine-cell profiles are found at many dyad synapses onto M5 cells, some of these derived from amacrine processes that extend horizontally for hundreds of microns.

Horizontal cell feedback contributes to chromatic opponency in some ganglion cells, but this seems not to be the primary mechanism in M5 cells. Blocking such feedback with HEPES buffer depressed overall surround antagonism somewhat, but did not fundamentally alter chromatic opponency (Fig 3M, N). Nor does melanopsin play any obvious role in the chromatic opponency, which persisted in M5 cells recorded in melanopsin knockout retinas. Contributions from the intrinsic response should be spatially restricted to the somadendritic profile of the cells and thus to the receptive-field center. There, it might boost the synaptically-mediated center response, especially for blue visible wavelengths and for strong, steady illumination. However, such contributions are presumably modest, as the melanopsin-based intrinsic photoresponse is far weaker (~10 pA) than the synaptically-mediated light response (hundreds of pA).

Relation to earlier findings on chromatic coding in mice and other species

Among extracellularly recorded mouse retinal ganglion cells, about 2% had S-ON and M-OFF responses to full-field stimuli (Ekesten and Gouras, 2005). These may have been M5 cells, but their morphology was not determined. In the opsin transition zone, some alpha-like ganglion cells in mice exhibit S-ON/M-OFF color opponency (Chang et al., 2013). These are distinct from the M5 cells reported here, which have smaller somas and more compact, highly branched dendritic arbors than alpha cells, including the M4 ("ON-alpha") ipRGCs (Estevez et al., 2012; see also Fig. 1 and Table 1). Moreover, chromatic opponency is present in M5 cells located far from the opsin transition zone.

Short-wavelength-preferring color opponent retinal ganglion cells have been documented in various other dichromatic mammals including the cat, guinea pig, ground squirrel, and rabbit, as well as in trichromatic non-human primates, but their form and the synaptic basis of their opponency vary widely, and none strongly resembles the M5 cell in mice (see (Marshak and Mills, 2014) for review). In particular, the chromatically opponent center-surround mechanism in M5 cells differs from opponency generated by sign-inverting amacrine cells as demonstrated previously in the mouse (Chang et al., 2013), guinea pig (Yin et al., 2009), ground squirrel (Sher and DeVries, 2012), and rabbit (Mills et al., 2014) in either S+/M− or M+/S− opponent RGCs. It also differs from two types of color opponent cells in primates: the center-only S+/(LM)− small bistratified cell and the (LM)+/S− chromatically opponent ipRGC described in monkeys (Dacey et al., 2014; Dacey and Lee, 1994; Dacey et al., 2005). While it is generally agreed that blue-yellow opponency is the ancestral form of chromatic coding in mammalian visual systems, it appears to be implemented in different ways by different cell types among extant mammals (Marshak and Mills, 2014; Solomon and Lennie, 2007)

Role in visual function

Though ipRGCs are typically associated with non-image-forming functions such as circadian photoentrainment and the pupillary light reflex, some subtypes also innervate the dLGN and influence the visual cortex, and we show that M5 cells are among those linked to the cortical visual pathway. It seems likely the chromatic opponency of M5 cells is maintained to some extent at the geniculate and cortical level and that it could therefore contribute the mouse's behavioral capacity for chromatic discrimination (Jacobs et al., 2004). A minority of neurons in both the dLGN and visual cortex of mice exhibit chromatic signals that are not readily explained by the dorsoventral opsin gradient, and some of these share the M5 cells' UV+/M− wavelength preference (Aihara et al., 2017; Denman et al., 2017; Ekesten and Gouras, 2008; Tan et al., 2015). UV-selective geniculate neurons exhibit relatively sustained responses compared to mouse dLGN neurons generally (Denman et al., 2017), mirroring the sustained responses of M5 cells.

In murine visual cortex, UV-preferring neurons are found even in the representation of the inferior visual field (dorsal retina), where the predominant cone type expresses mainly M-opsin. M5 cells, which similarly prefer UV over green stimuli throughout the retina are a plausible source of excitatory geniculocortical drive for such UV-preferring cortical neurons. Overall, however, the interrelationships among color-selective neurons at retinal, thalamic and cortical levels remain unclear in mice, as in primates (Solomon and Lennie, 2007).

Thus, while M5 cells share melanopsin expression and intrinsic photosensitivity with other ipRGCs, their synaptically-driven properties and brain projections implicate them in mechanisms of visual perception, especially color vision. This adds to growing evidence that image-forming and non-image-forming pigments, cell types, and circuits are not as distinct as once imagined. A possible role for M5 cells in non-image-forming functions is not excluded, especially because the central projections beyond those to the dLGN described here remain to be determined. Some mouse SCN neurons have recently been reported to exhibit cone-dependent blue-on/yellow-off spectral opponency (Walmsley et al., 2015).

Chromatic cues could provide a more reliable indication of time of day than changes in ambient illumination alone. Could M5 cells be the source of such chromatic information influencing the circadian system? Retinal input to the mouse SCN is thought to derive from chromatically unselective M1 and M2 subtypes of ipRGCs (Berson et al., 2002; Hattar et al., 2006; Hattar et al., 2002). However, the intergeniculate nucleus, a component of the LGN complex, projects to the SCN in some mammals (Harrington, 1997), providing a possible route by which M5 cells might indirectly supply chromatic information to the circadian pacemaker.

STAR Methods

CONTACT FOR REAGENT AND RESOURCE SHARING

Further information and requests for resources and reagents should be directed to and will be fulfilled by the Lead Contact, Maureen Estevez Stabio (maureen.stabio@ucdenver.edu).

EXPERIMENTAL MODEL AND SUBJECT DETAILS

Animals—Experiments were conducted under protocols approved by the Animal Care and Use Committee at Brown University and in accordance with NIH guidelines. Male and female adult mice (1 to 3 months of age) from a melanopsin reporter line, Opn4$^{cre/+}$;Z/EG$^{+/-}$, were used to target M5 cells and other ipRGCs for study (Ecker et al., 2010; Estevez et al., 2012); these mice express enhanced green fluorescent protein (EGFP) in ipRGCs. In some experiments, to isolate synaptically-driven light responses from those generated by cell-autonomous melanopsin phototransduction, we used mice which ipRGCs express EGFP instead of melanopsin (Opn4$^{cre/cre}$;Z/EG$^{+/-}$). Mice housed in animal care facilities at Brown University and maintained on a 12 hr: 12 hr light-dark cycle with food and water ad libitum.

METHOD DETAILS

Tissue preparation and solutions—Whole-mounted retinas were prepared for experiments as described previously (Estevez et al., 2012). Mice were killed by CO_2 inhalation followed by cervical dislocation. We kept track of retinal orientation by making a prominent relieving cut through the dorsal margin of the eyecup. This was guided by a small cautery mark made prior to enucleation on the dorsal corneal margin equidistant from the temporal and nasal canthi. Retinas were removed under dim red illumination and mounted in a glass chamber, with the ganglion-cell layer facing upwards. The retina was superfused at 2mL/min with Ames' medium (Sigma), supplemented with 23mM $NaHCO_3$ and 10mM D-glucose, bubbled with 95% O_2/5% CO_2 and maintained at 30–35°C. Intracellular solutions used for electrophysiological recordings contained (in mM): 120 K-gluconate (for current-clamp) or Cs-methanesulfonate (for voltage-clamp), 5 NaCl, 4 KCl or CsCl, 2 EGTA, 10 HEPES, 4 ATP-Mg, 7 phosphocreatine-Tris, 0.3 GTP-Tris and 2 QX-314 (for voltage clamp only), pH 7.3, 270–280 mOsm. We revealed cellular morphology by dye filling with Lucifer Yellow or Alexa-488 hydrazide. These dyes were introduced either by passive diffusion during patch clamp experiments or by intracellular dye injections using sharp micropipettes (Pu et al., 1994). To block synaptic communication from outer to inner retina, we used a cocktail consisting of 100 μM L-(+)-2-amino-4-phosphonobutyric acid (L-AP4, a group III metabotropic glutamate receptor agonist), 40 μM 6, 7-dinitroquinoxaline-2, 3-dione (DNQX,

an AMPA/kainate receptor antagonist), and 30 μM D-(−)-2-amino-5-phosphonopentanoic acid (D-AP5, an NMDA receptor antagonist). In other experiments a cocktail of 50 μM 1, 2, 5, 6-Tetrahydropyridin-4-yl methylphosphinic acid (TPMPA; a $GABA_C$ receptor antagonist) and 20 μM gabazine (a $GABA_A$ receptor antagonist) was used to block ionotropic GABAergic inhibition; strychnine (10 μM) was used for blocking glycinergic transmission (Rajendra et al., 1997); and tetrodotoxin (TTX, 500 nM) was used for blocking voltage-gated Na^+ channels (Hu et al., 2013; Reifler et al., 2015; Wong et al., 2007). Horizontal cell to cone feedback was blocked by the addition of 10 mM HEPES (4-(2-hydroxyethyl)-1-piperazineethanesulfonic acid) to the extracellular solution (Cadetti and Thoreson, 2006; Thoreson et al., 2008). For those experiments, the pH of the HEPES-containing solution was adjusted to 7.4 using 1 M NaOH to match that of the control bicarbonate-buffered Ames solution, while bubbling with 95% O_2 – 5% CO_2.

Electrophysiology—Whole-cell patch clamp recordings were performed using an Axopatch 700B amplifier, Digidata 1322 digitizer, and pClamp 9.2 data acquisition software (Molecular Devices, Sunnyvale, CA). A sampling frequency of 10 kHz was used. Recordings were low-pass filtered at 4kHz. A Flaming/Brown P-97 pipette puller (Sutter Instruments, Novato, CA) was used to make borosilicate patch pipettes that had tip resistances between 4- 8 M when filled with intracellular solution.

EGFP+ cells were identified by mercury epifluorescence (460 – 500 nm), and then targeted for whole-cell patch recording under infrared optics. Thus, all subsequent photic responses - although recorded in darkness - were with the retina in a strongly bleach-adapted state due to the initial exposure to bright epifluorescent light (see Fig. 5 of Estevez et al., 2012). Series resistance for voltage clamp recordings was always under 30 MΩ. Cells were voltage clamped at -64 mV after correction for liquid junction potential as in Estevez et al., 2012. Full-field light steps (1 s for tests of synaptically-driven responses; 5 or 10s for melanopsin-dependent responses) were delivered using the beam of a 100W xenon lamp passed through neutral density and bandpass filters mounted on dual filter wheels (MAC 5000, Ludl Electronic Products, Hawthorne, NY) and gated with an electronically controlled shutter. The irradiances of unattenuated light at 360, 480, and 520 nm were $1.7 \cdot 10^{16}$, $2.9 \cdot 10^{17}$, and $3.9 \cdot 10^{17}$ photons $\cdot$ cm^{-2} $\cdot$ s^{-1}, respectively. In some experiments we introduced an iris into the xenon illumination path to spatially restrict such stimuli to smaller spots (either 165 μm or 620 μm diameter at the retinal surface). Electrophysiological data were analyzed using Clampfit 10.3 (Molecular Devices, Sunnyvale, CA) and Origin 6.0 (Microcal Software, Northampton, MA).

Immunohistochemistry and antibodies—Immunohistochemical protocols were as reported previously (Estevez et al., 2012) and described here: Retinas were fixed for 1 h in 4% paraformaldehyde (PFA) in 0.1 M phosphate buffer (PBS), then rinsed in 0.1 M PBS (6 × 10 min). Retinas were soaked overnight at 4°C in a PBS solution of 2% Triton X-100 and 5% donkey serum, then incubated for two days at 4°C in primary antibody, rinsed in PBS (6 × 10 min), then incubated for 2-4 hrs at 4°C in secondary antibody and finally washed in PBS (3 × 15 min). The primary antibodies were goat polyclonal anti-choline acetyltransferase (1:200; ChAT; Millipore, Temecula, CA) and rabbit polyclonal anti-

melanopsin (1:10,000; ATS-Advanced Targeting Systems, San Diego, CA). Secondary antibodies were Alexa Fluor 594 or 647 donkey anti-goat IgG and Alexa Fluor donkey anti-rabbit 594 (1:200; Invitrogen-Molecular Probes, Eugene, OR). In some cases, the sensitivity of melanopsin immunodetection was increased by tyramide signal amplification with horseradish peroxidase (HRP)-tagged goat anti-rabbit IgG and Alexa Fluor 594 tyramide (TSA-15, Molecular Probes, Eugene, OR), using the manufacturer's protocol exactly with the exception of PerkinElmer 1X Plus Amplification Diluent which replaced the diluent included in the kit. Retinas were mounted on glass slides and coverslipped using Aqua-Mount or ProLong Gold (Invitrogen, Carlsbad, CA)

Serial block face electron microscopy—To characterize the bipolar-cell inputs to M5 cells, we analyzed two sets of serial electron microscopic sections of adult mouse retina. The first of these (e2006) is the volume introduced and comprehensively analyzed by Helmstaedter and colleagues and made freely available online (Helmstaedter et al., 2013). This volume was processed to suppress intracellular detail, including synaptic specializations, in favor of highlighting the extracellular space to facilitate exhaustive segmentation. Supplemental material in the paper includes detailed reconstructions of every bipolar cell and ganglion cell in the volume and the amount of surface contact between any two cells, an indirect measure of presumptive synaptic contact. The second volume (k0725) is described in detail elsewhere (Ding et al., 2016). It was obtained from a young adult mouse (C57BL/6; 30 days of age), and fixed for 2 h at room temperature in 2% buffered glutaraldehyde. A 1 mm^2 sample obtained roughly midway between optic disk and retinal margin was excised, stained with heavy metals to reveal synaptic ribbons and vesicles and other intracellular detail, dehydrated, and embedded in Epon Hard. A trimmed block (~200 μm × 400 μm) was imaged in a scanning electron microscope with a field-emission cathode (QuantaFEG 200, FEI Company). Back-scattered electrons were detected using a custom-designed detector and custom-built current amplifier. The incident electron beam delivered about 10 electrons/nm^2. Imaging was performed at high vacuum. Sides of the block were evaporation-coated with gold. The block face was serially cut as described elsewhere (Helmstaedter et al., 2013). Using a 26 nm section thickness 10112 consecutive block faces were imaged, yielding aligned data volumes of 4992 × 16000 × 10112 voxels (1 × 5 mosaic of 3584 × 3094 images). This corresponds to a spatial volume of approximately 50 × 210 × 260 μm. The smallest dimension corresponds to retinal depth, which ranged from the ganglion cell layer to the innermost part of the inner nuclear layer. The edges of neighboring mosaic images overlapped by ~1 μm. Mosaics and slices were aligned off-line to subpixel precision by Fourier shift-based interpolation. The data sets were then split into cubes (128 × 128 × 128 voxels) for import into KNOSSOS (www.knossostool.org), a freely available software package for exploration and skeletonization of cell profiles in SBEM datasets. We also used open-source software for manual segmentation (ITK-Snap), and for three-dimensional displays of profiles of interest (ParaView).

Intravitreal eye injections—Mice were anesthetized with isoflurane (3% in oxygen; Matrx VIP 3000, Midmark). A viral vector designed for Cre-dependent cell labeling with GFP (AAV2-CAG-Flex-GFP; Vector Core, UNC http://www.med.unc.edu/genetherapy/vectorcore, which can be found under AAV In Stock Vectors: Ed Boyden > Control Vectors

Serotype 2; AAV-CAG-FLEX-GFP; 1.5 –2 μl of ~3.7 × 10^{12} units/ml) was injected into the vitreous humor of the right eye through a glass pipette using a microinjector (Picospritzer III, Science Products GmbH). Two weeks following the intravitreal injections, animals were subjected to intracranial injections of fluorescent beads into the dLGN. A week later, animals were killed and retinas and brains harvested.

Brain Injections—To determine whether M5 ipRGCs innervate the dLGN, we combined retrograde transport of fluorescent tracers with contrasting fluorescent tags marking melanopsin-expressing cells and revealing their somadendritic architecture. For these studies, mice were anesthetized by inhalation of 3% isoflurane and placed in a stereotaxic apparatus. Retrograde tracer (100–300 nL) was injected into the dLGN through a glass micropipette by pulses of pneumatic pressure.

Two variants of the method were used. In one set of experiments, we used the retrograde tracer cholera toxin β-subunit conjugated to Alexa Fluor 594 (CTB-594). This was injected unilaterally into the dLGN of Opn4$^{Cre/+}$;Z/EG$^{+/-}$ mice. One or more days post-injection, mice were euthanized and contralateral retinas were isolated and maintained in a superfusion chamber. EGFP-positive presumptive ipRGCs that were also retrolabeled were dye-filled by intracellular injection as described (Estevez et al., 2012). In a second experimental series, we used an alternative retrograde tracer (rhodamine latex microspheres [Lumafluor] diluted to half the stock concentration with water) and injected into the dLGN of Opn4$^{Cre/+}$ mice. Two to four weeks previously, these mice had received an intraocular injection through a glass pipette using a microinjector (Picospritzer III, Science Products GmbH) of one of two flexed (Cre-dependent) viruses into the eye contralateral to the dLGN injection, triggering intense GFP fluorescence in the membranes of Cre-expressing cells (i.e., ipRGCs). GFP (AAV2-CAG-Flex-GFP; Vector Core, UNC; 1.5 –2 μL of ~3.7 × 10^{12} units/ml) was injected into the vitreous humor of the right eye.

Brains were removed, submerged in 4% paraformaldehyde overnight, rinsed in phosphate buffer, and embedded in agarose. Coronal sections were cut at 50 μm on a vibratome (Leica VT100S) and mounted on glass slides with Aqua-Mount. The location and specificity of the injection site was confirmed using epifluorescence and bright field imaging of brain sections as well as topographic evaluation of the retrograde retinal labeling pattern.

Imaging—Dye-filled cells were digitally imaged on an epifluorescence microscope (Berson et al., 2010; Ecker et al., 2010). Confocal images were acquired with either a Zeiss LSM 510 Meta or Zeiss 800 laser scanning microscope and analyzed using either Zeiss LSM Image Browser or Zen 2 software. Dye-filled cells were manually reconstructed, measured, and analyzed using ImageJ and Adobe Photoshop as described previously (Estevez et. al., 2012). Confocal z-stacks from selected dye-filled cells were computationally processed to normalize depth relative to the choline acetyltransferase (ChAT) immunopositive laminae, as pioneered by others (Sümbül et al., 2014). Custom Matlab software incorporated code from Sümbül and colleagues for automated detection of the ChAT bands, permitted iterative fine-tuning of depth assignments by the user, and also normalized the depth difference between the ON and OFF ChAT bands. These corrected z-stacks were used to generate plots of dendritic depth (integrated signal strength as a function

of z) and warp-corrected orthogonal projections, using the Plot Z Axis Profile and Orthogonal Views stack functions of ImageJ (Fig. 1).

When using Cre-dependent viruses to assess the morphology of ipRGCs retrolabeled from the dLGN, we reconstructed the somadendritic profiles of individual cells by carefully tracing individual labeled processes through high resolution confocal z-stacks. Ambiguity could arise Where two labeled processes were closely apposed, ambiguity could arise about which process represented the continuation of the process being traced. As in a prior study (Berson et al., 2010), we were often able to resolve this ambiguity by careful assessment of process caliber, form, staining intensity, and depth, and by the tendency of processes to follow relatively straight courses. Where substantial uncertainty remained (typically for finer distal dendrites), we terminated the tracing at that point. Thus, these reconstructions are surely incomplete.

Modeling cone opsin contributions—We generated a simple model to probe the relative contribution of the mouse's two cone photopigments to the excitatory center response of M5 cells. We assumed equivalent photon-flux activation thresholds for these pigments at their best wavelength (λ_{max}). Relative sensitivities of the two opsins for any monochromatic stimulus were derived from opsin template functions (Lamb, 1995) set to peak sensitivities of 360 nm (for UV opsin) and 510 nm (for the mid-wavelength cone opsin). The excitatory effect of monochromatic light acting through a single pigment system to excite the M5 cell was modeled as sigmoidal saturating function of light intensity, using the Michaelis-Menten equation. A fixed gain term (exponent = 1.5) gave a good fit to the slope of the empirically determined irradiance-response functions across all conditions. The net irradiance-response behavior of the M5 center mechanism for a specific monochromatic wavelength was modeled as the weighted sum of the fractional contributions from each pigment system. This fraction was the only free parameter in the model.

QUANTIFICATION AND STATISTICAL ANALYSIS

Morphological data in Table 1 are shown as mean ± standard deviation, where n represents number of cells. Morphological comparisons between ipRGC subtypes were significant when $p < 0.05$, as determined by an independent two-tailed Student's t-test performed in Origin Pro 2016. Analysis of physiological data was performed in Clampfit 10.3 and MatLab. Data plotted in Figure 3 are mean ± standard error of mean. Our physiological data violated both the normality and homoscedasticity assumptions. Therefore, we utilized t-test for two independent samples using percentile bootstrap methods (Wilcox and Rousselet, 2017). Specifically, we used the difference between the bootstrap-sampled medians of the two groups as a test statistic (d). If the 95% confidence interval of d does not include zero, the medians of the two groups are significantly different.

DATA AND SOFTWARE AVAILABILITY

An analysis program to flatten retinal image stacks using CHaT bands (Figure 1A) was developed based on code from Sümbül et al., 2014 and is freely available at the following URL: https://github.com/mschiel/retinal-flattener

Supplementary Material

Refer to Web version on PubMed Central for supplementary material.

Acknowledgments

References

Aihara S, Yoshida T, Hashimoto T, Ohki K. Color Representation Is Retinotopically Biased but Locally Intermingled in Mouse V1. Front Neural Circuits. 2017; 11:22. [PubMed: 28405186]

Baden T, Berens P, Franke K, Román Rosón M, Bethge M, Euler T. The functional diversity of retinal ganglion cells in the mouse. Nature. 2016; 529:345–350. [PubMed: 26735013]

Behrens C, Schubert T, Haverkamp S, Euler T, Berens P. Connectivity map of bipolar cells and photoreceptors in the mouse retina. Elife. 2016; 5

Berson DM, Castrucci AM, Provencio I. Morphology and mosaics of melanopsin-expressing retinal ganglion cell types in mice. J Comp Neurol. 2010; 518:2405–2422. [PubMed: 20503419]

Berson DM, Dunn FA, Takao M. Phototransduction by retinal ganglion cells that set the circadian clock. Science. 2002; 295:1070–1073. [PubMed: 11834835]

Bleckert A, Schwartz GW, Turner MH, Rieke F, Wong RO. Visual space is represented by nonmatching topographies of distinct mouse retinal ganglion cell types. Curr Biol. 2014; 24:310–315. [PubMed: 24440397]

Cadetti L, Thoreson WB. Feedback effects of horizontal cell membrane potential on cone calcium currents studied with simultaneous recordings. J Neurophysiol. 2006; 95:1992–1995. [PubMed: 16371457]

Chang L, Breuninger T, Euler T. Chromatic coding from cone-type unselective circuits in the mouse retina. Neuron. 2013; 77:559–571. [PubMed: 23395380]

Dacey DM, Crook JD, Packer OS. Distinct synaptic mechanisms create parallel S-ON and S-OFF color opponent pathways in the primate retina. Vis Neurosci. 2014; 31:139–151. [PubMed: 23895762]

Dacey DM, Lee BB. The 'blue-on' opponent pathway in primate retina originates from a distinct bistratified ganglion cell type. Nature. 1994; 367:731–735. [PubMed: 8107868]

Dacey DM, Liao HW, Peterson BB, Robinson FR, Smith VC, Pokorny J, Yau KW, Gamlin PD. Melanopsin-expressing ganglion cells in primate retina signal colour and irradiance and project to the LGN. Nature. 2005; 433:749–754. [PubMed: 15716953]

Denman DJ, Siegle JH, Koch C, Reid RC, Blanche TJ. Spatial Organization of Chromatic Pathways in the Mouse Dorsal Lateral Geniculate Nucleus. J Neurosci. 2017; 37:1102–1116. [PubMed: 27986926]

Dhande OS, Huberman AD. Retinal ganglion cell maps in the brain: implications for visual processing. Curr Opin Neurobiol. 2014; 24:133–142. [PubMed: 24492089]

Ding H, Smith RG, Poleg-Polsky A, Diamond JS, Briggman KL. Species-specific wiring for direction selectivity in the mammalian retina. Nature. 2016; 535:105–110. [PubMed: 27350241]

Ecker JL, Dumitrescu ON, Wong KY, Alam NM, Chen SK, LeGates T, Renna JM, Prusky GT, Berson DM, Hattar S. Melanopsin-expressing retinal ganglion-cell photoreceptors: cellular diversity and role in pattern vision. Neuron. 2010; 67:49–60. [PubMed: 20624591]

Ekesten B, Gouras P. Cone and rod inputs to murine retinal ganglion cells: evidence of cone opsin specific channels. Vis Neurosci. 2005; 22:893–903. [PubMed: 16469196]

Ekesten B, Gouras P. Cone inputs to murine striate cortex. BMC Neurosci. 2008; 9:113. [PubMed: 19014590]

Estevez ME, Fogerson PM, Ilardi MC, Borghuis BG, Chan E, Weng S, Auferkorte ON, Demb JB, Berson DM. Form and function of the M4 cell, an intrinsically photosensitive retinal ganglion cell type contributing to geniculocortical vision. J Neurosci. 2012; 32:13608–13620. [PubMed: 23015450]

Harrington ME. The ventral lateral geniculate nucleus and the intergeniculate leaflet: interrelated structures in the visual and circadian systems. Neurosci Biobehav Rev. 1997; 21:705–727. [PubMed: 9353800]

Hattar S, Kumar M, Park A, Tong P, Tung J, Yau KW, Berson DM. Central projections of melanopsin-expressing retinal ganglion cells in the mouse. J Comp Neurol. 2006; 497:326–349. [PubMed: 16736474]

Hattar S, Liao HW, Takao M, Berson DM, Yau KW. Melanopsin-containing retinal ganglion cells: architecture, projections, and intrinsic photosensitivity. Science. 2002; 295:1065–1070. [PubMed: 11834834]

Helmstaedter M, Briggman KL, Turaga SC, Jain V, Seung HS, Denk W. Connectomic reconstruction of the inner plexiform layer in the mouse retina. Nature. 2013; 500:168–174. [PubMed: 23925239]

Hu CP, Hill DD, Wong KY. Intrinsic physiological properties of the five types of mouse ganglion-cell photoreceptors. Journal of Neurophysiology. 2013; 109:1876–1889. [PubMed: 23343892]

Jacobs GH, Williams GA, Fenwick JA. Influence of cone pigment coexpression on spectral sensitivity and color vision in the mouse. Vision Res. 2004; 44:1615–1622. [PubMed: 15135998]

Lamb TD. Photoreceptor spectral sensitivities: common shape in the long- wavelength region. Vision Res. 1995; 35:3083–3091. [PubMed: 8533344]

Marshak DW, Mills SL. Short-wavelength cone-opponent retinal ganglion cells in mammals. Vis Neurosci. 2014; 31:165–175. [PubMed: 24759445]

Mills SL, Tian LM, Hoshi H, Whitaker CM, Massey SC. Three distinct blue-green color pathways in a mammalian retina. J Neurosci. 2014; 34:1760–1768. [PubMed: 24478358]

Pfeiffenberger C, Yamada J, Feldheim DA. Ephrin-As and patterned retinal activity act together in the development of topographic maps in the primary visual system. J Neurosci. 2006; 26:12873–12884. [PubMed: 17167078]

Pu M, Berson DM, Pan T. Structure and function of retinal ganglion cells innervating the cat's geniculate wing: an in vitro study. J Neurosci. 1994; 14:4338–4358. [PubMed: 8027783]

Rajendra S, Lynch JW, Schofield PR. The glycine receptor. Pharmacol Ther. 1997; 73:121–146. [PubMed: 9131721]

Reifler AN, Chervenak AP, Dolikian ME, Benenati BA, Li BY, Wachter RD, Lynch AM, Demertzis ZD, Meyers BS, Abufarha FS, et al. All spiking, sustained ON displaced amacrine cells receive gap-junction input from melanopsin ganglion cells. Current Biology. 2015; 25:2878–2878.

Rhim I, Coello-Reyes G, Ko HK, Nauhaus I. Maps of cone opsin input to mouse V1 and higher visual areas. J Neurophysiol. 2017; 117:1674–1682. [PubMed: 28100658]

Schmidt TM, Alam NM, Chen S, Kofuji P, Li W, Prusky GT, Hattar S. A role for melanopsin in alpha retinal ganglion cells and contrast detection. Neuron. 2014; 82:781–788. [PubMed: 24853938]

Schmidt TM, Chen SK, Hattar S. Intrinsically photosensitive retinal ganglion cells: many subtypes, diverse functions. Trends Neurosci. 2011; 34:572–580. [PubMed: 21816493]

Schmidt TM, Kofuji P. Functional and morphological differences among intrinsically photosensitive retinal ganglion cells. J Neurosci. 2009; 29:476–482. [PubMed: 19144848]

Schmidt TM, Kofuji P. Differential cone pathway influence on intrinsically photosensitive retinal ganglion cell subtypes. J Neurosci. 2010; 30:16262–16271. [PubMed: 21123572]

Schmidt TM, Kofuji P. Structure and function of bistratified intrinsically photosensitive retinal ganglion cells in the mouse. J Comp Neurol. 2011; 519:1492–1504. [PubMed: 21452206]

Schwartz GW, Okawa H, Dunn FA, Morgan JL, Kerschensteiner D, Wong RO, Rieke F. The spatial structure of a nonlinear receptive field. Nat Neurosci. 2012; 15:1572–1580. [PubMed: 23001060]

Sher A, DeVries SH. A non-canonical pathway for mammalian blue-green color vision. Nat Neurosci. 2012; 15:952–953. [PubMed: 22634728]

Solomon SG, Lennie P. The machinery of colour vision. Nat Rev Neurosci. 2007; 8:276–286. [PubMed: 17375040]

Author Manuscript Author Manuscript Author Manuscript Author Manuscript

Sonoda T, Schmidt TM. Re-evaluating the Role of Intrinsically Photosensitive Retinal Ganglion Cells: New Roles in Image-Forming Functions. Integr Comp Biol. 2016; 56:834–841. [PubMed: 27371393]

Sümbül U, Song S, McCulloch K, Becker M, Lin B, Sanes JR, Masland RH, Seung HS. A genetic and computational approach to structurally classify neuronal types. Nat Commun. 2014; 5:3512. [PubMed: 24662602]

Tan Z, Sun W, Chen TW, Kim D, Ji N. Neuronal Representation of Ultraviolet Visual Stimuli in Mouse Primary Visual Cortex. Sci Rep. 2015; 5:12597. [PubMed: 26219604]

Thoreson WB, Babai N, Bartoletti TM. Feedback from horizontal cells to rod photoreceptors in vertebrate retina. J Neurosci. 2008; 28:5691–5695. [PubMed: 18509030]

Völgyi B, Chheda S, Bloomfield SA. Tracer coupling patterns of the ganglion cell subtypes in the mouse retina. J Comp Neurol. 2009; 512:664–687. [PubMed: 19051243]

Walmsley L, Hanna L, Mouland J, Martial F, West A, Smedley AR, Bechtold DA, Webb AR, Lucas RJ, Brown TM. Colour as a signal for entraining the mammalian circadian clock. PLoS Biol. 2015; 13:e1002127. [PubMed: 25884537]

Wässle H, Puller C, Müller F, Haverkamp S. Cone contacts, mosaics, and territories of bipolar cells in the mouse retina. J Neurosci. 2009; 29:106–117. [PubMed: 19129389]

Weng S, Estevez ME, Berson DM. Mouse ganglion-cell photoreceptors are driven by the most sensitive rod pathway and by both types of cones. PLoS One. 2013; 8:e66480. [PubMed: 23762490]

Wilcox RR, Rousselet GA. A guide to robust statistical methods in neuroscience. bioRxiv. 2017

Wong KY, Dunn FA, Graham DM, Berson DM. Synaptic influences on rat ganglion-cell photoreceptors. Journal of Physiology-London. 2007; 582:279–296.

Yin L, Smith RG, Sterling P, Brainard DH. Physiology and morphology of color-opponent ganglion cells in a retina expressing a dual gradient of S and M opsins. J Neurosci. 2009; 29:2706–2724. [PubMed: 19261865]

Zhao X, Stafford BK, Godin AL, King WM, Wong KY. Photoresponse diversity among the five types of intrinsically photosensitive retinal ganglion cells. J Physiol. 2014; 592:1619–1636. [PubMed: 24396062]
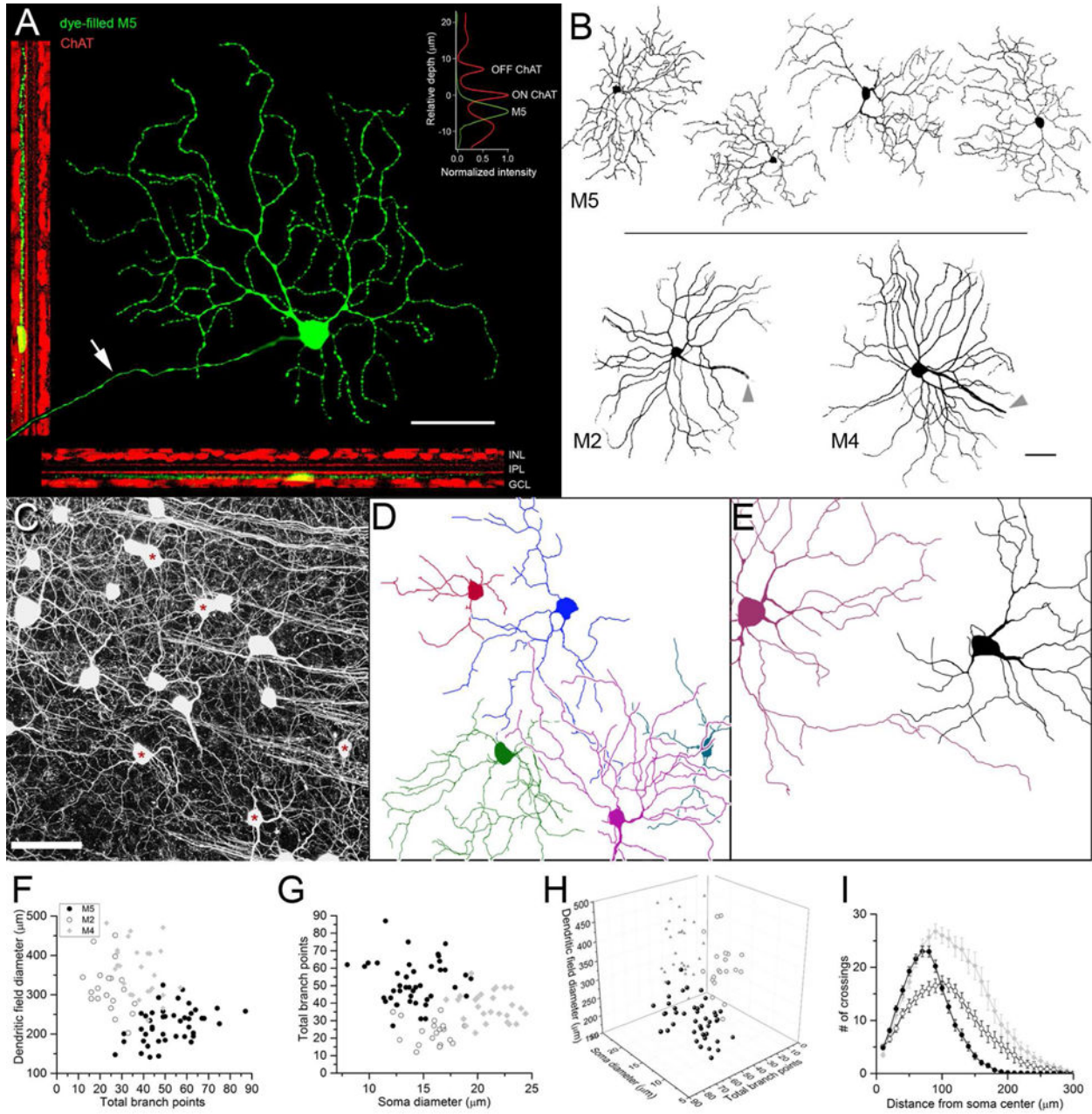
Fig. 1. Morphology and mosaic of M5 ipRGCs in relation to M2 and M4 (ON-alpha) cells
The only other known ipRGC subtypes with dendritic arbors monostratified in the ON sublayer. (**A**) dendritic branching and stratification of a single representative M5 cell. Central green profile is a maximum-intensity-projected confocal image of an M5 cell targeted for *in vitro* patch recording based on EGFP labeling in an Opn4$^{cre/+}$;Z/EG$^{+/-}$ retina and filled with Lucifer yellow (green) during patch recording. Arrow indicates axon. Digitally flattened and rotated views of same cell shown in two narrow panels to the left and bottom; dendrites ramify proximal to (below) the ON ChAT band (red, anti-ChAT), close to the ganglion cell layer. Top right inset: Intensity profiles plotting relative depth within IPL of

M5 dendrites (green) compared to the ChAT bands (red). (**B**) Dendritic arbors of four M5 ipRGCs (top) compared to representative M2 and M4 cells (bottom), all viewed *en face* at same magnification. Cells dye-filled during patch recordings or by iontophoresis through sharp micropipettes were imaged by confocal microscopy. Maximum-intensity projections were converted to gray scale, inverted, and masked to show only the dye-filled cell. Arrowheads indicate axons. (**C–E**) Partial reconstruction of the mosaic of M5 cells in a sample (250×250 μm) of a flat-mounted retina from an Opn4$^{cre/}$+;Z/EG$^{+/−}$ mouse. (**C**) Maximum intensity projection of GFP fluorescence in ipRGCs in confocal optical sections spanning mid-IPL through the ganglion cell layer. (**D**) Partial reconstruction of dendritic arbors of 5 presumed M5 cells within this same field (somas marked by asterisks in **C**). All were monostratified in the inner ON sublayer and too highly branched to be M2 or M4 cells. Dendritic profiles are certainly incomplete because tracing was truncated wherever there was doubt about which of two possible extensions belonged to the traced cell. Even so, dendrites of these cells appear to tile the retina with substantial overlap. (**E**) Partial reconstruction of two M4 cells in same field, for comparison. (**F–I**) Morphology of M5 cells compared with those of M2 and M4 ipRGCs (replotted from Estevez et al., 2012). (**F**) Dendritic field diameter versus total branch points. (**G**) Total branch points versus soma diameter. (**H**) Three-dimensional plot of parameters in (F) and (G) viewed from the perspective best separation among clusters of M5, M2 and M4 cells. (**I**) Sholl analysis of dendritic branching pattern; error bars represent SEM. Sample sizes for F–I: M2 = 20; M4 = 27; M5 = 44. See also Table 1. Scale bars in A, B and C = 50 μm
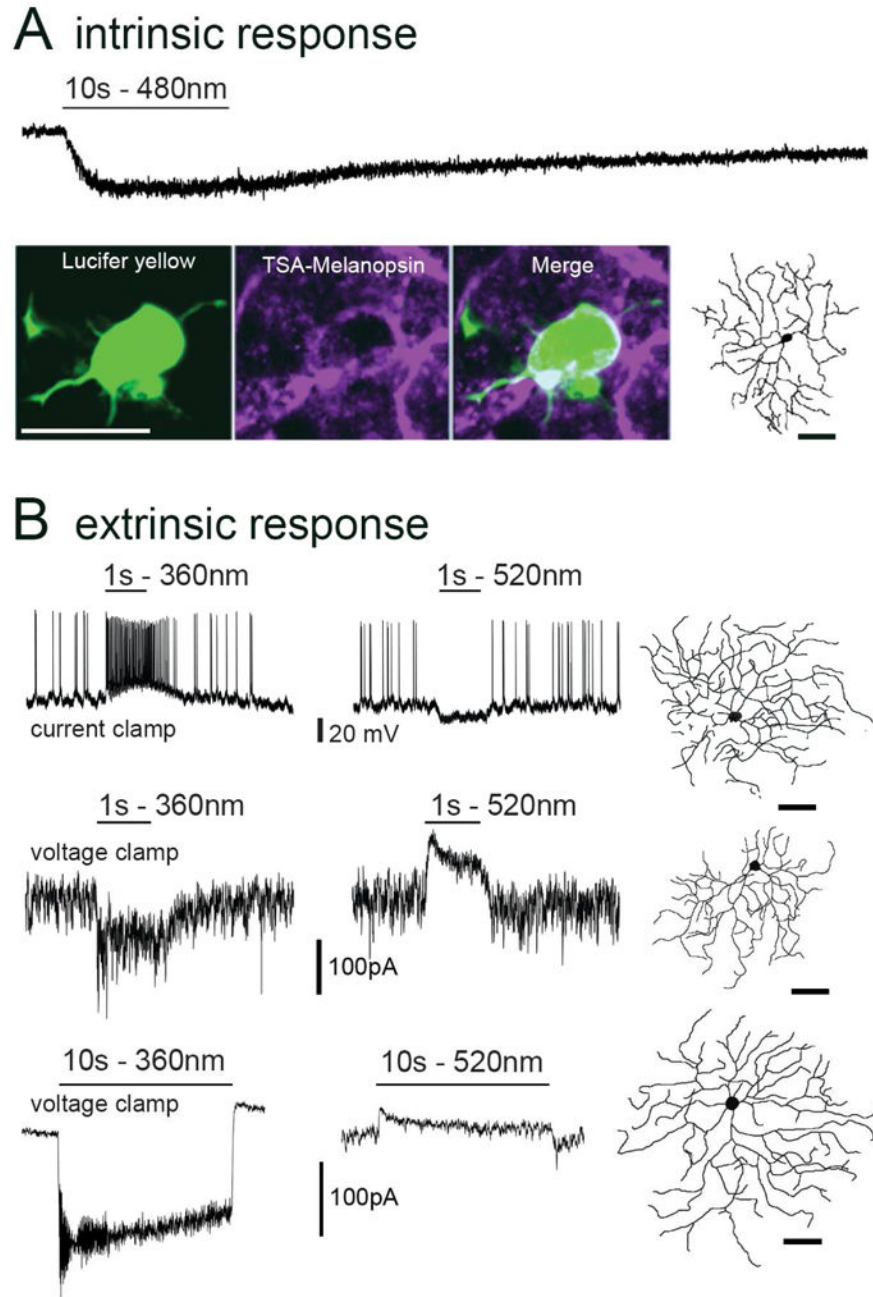
A intrinsic response

10s - 480nm

B extrinsic response

Fig. 2. Intrinsic and extrinsic photoresponses of M5 cells

(**A**) Intrinsic melanopsin-based response. Whole-cell voltage-clamp recording during pharmacological blockade of retinal synapses; note the slow inward current elicited by a 10s step of full-field 480 nm light of maximum intensity. Modest melanopsin immunofluorescence (purple) is detectable in the somatic membrane of an M5 cell after tyramide signal amplification. Same cell was dye-filled with Lucifer yellow (green) during recording (scale bar: 20 μm). Reconstructed profile reveals this cell's small bushy dendritic arbor (right; as in Fig. 1; scale bar = 50 μm). (**B**) Light-evoked voltage and current responses to diffuse full-field light steps of 1 s (middle traces) and 10 second (bottom traces) at two

different wavelengths optimized to activate either UV-cone opsin (360 nm, left column) M-cone opsin (520 nm, right column). Stimuli in left and right columns were matched in photon flux density (10^{16} photons $\cdot$ cm^{-2} $\cdot$ s^{-1} for current clamp recordings; 10^{14} photons $\cdot$ cm^{-2} $\cdot$ s^{-1} for voltage clamp; V_{hold} = -64mV). Morphological reconstructions of each recorded cell are shown at right (scale bar: 50 μm).
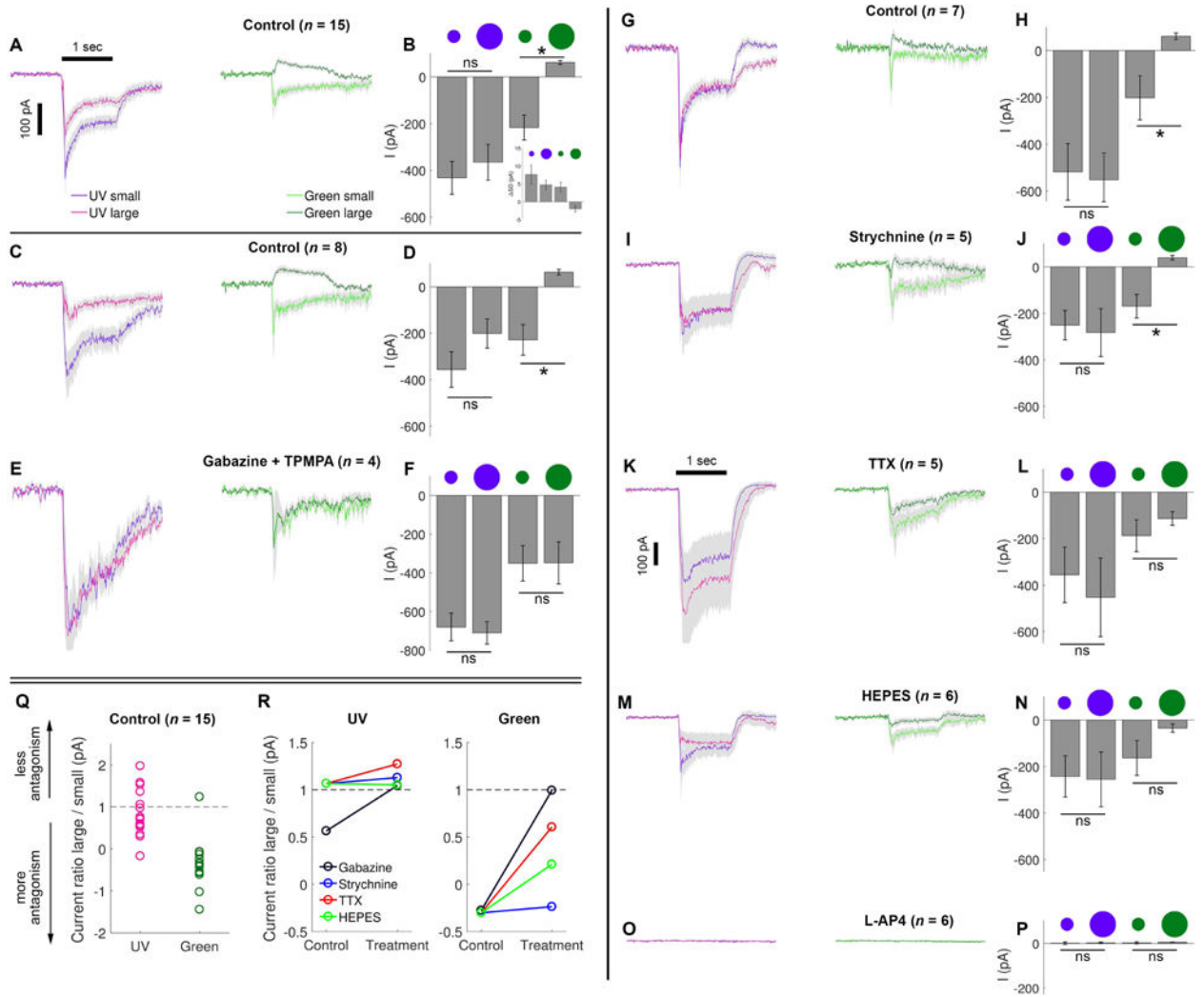
Fig. 3. Spatial receptive field organization and role of inhibition in chromatic opponency of M5 cells

(**A**) Light-evoked current responses of M5 cells to light spots of two sizes (165 μm or 620 μm diameter) and two wavelengths (360 nm, UV; or 520 nm, green) at matched irradiance. (**B**) Maximum light-evoked current (average ± SEM) of M5 cells for small or large spots of either wavelength. Inset in **B** shows spectral dependence of light-evoked changes in current noise, plotted as the change in standard deviation (SD) of the current during plateau of light response (last 0.5 s) evoked by the four light stimuli trials shown in A relative to the prestimulus baseline (0.5 s). Only large, longer-wavelength spots reduced current noise (see also responses to large green spots in panel **A**, suggesting pre-synaptic inhibitory mechanisms that suppresses tonic excitatory drive to the M5 cell. (**C–D**) Similar to **A** and **B**, but for subset #1 of control measurements. (**E–F**) Similar to **A** and **B**, but during bath application of antagonists of ionotropic GABA receptors (gabazine for GABA$_A$ and TPMPA for GABA$_C$). The outward current normally evoked by large green stimulus is abolished by blocking GABA transmission. (**G–H**) Similar to **A** and **B**, but for subset #2 of control measurements. (**I–P**) Similar to **A** and **B**, but during bath application of various pharmacological agents. (**I, J**) Strychnine, an antagonist of glycine receptors, left the light-

evoked responses similar to those in control bath. (**K, L**) Tetrodotoxin (TTX), a voltage-gated Na^+ channel antagonist, mimicked the effect of blocking GABAergic transmission. (**M, N**) HEPES, a pH buffer that suppresses horizontal cell feedback, reduced the surround suppression, but green stimuli remained more effective than UV ones in evoking the suppression. (**O, P**) The ON-channel blocker L-AP4 eliminated all synaptic responses to light. Current scale in A applies to all traces except K. (**Q**) The ratio of maximum light-evoked evoked current for large over small spots for either UV (left) or green (right) stimuli. Ratios ~1 indicate no surround antagonism, <1 indicates more antagonism, and >1 indicates surround facilitation. (**R**) Effect of the various pharmacological manipulations on the ratio of currents (large spot / small spot) in response to for either UV (left) or green (right) stimuli. Treatment groups were always compared to their matching control measurements. Error bars represent ± SEM. See also Figure S1 for cone opsin contribution to center responses.
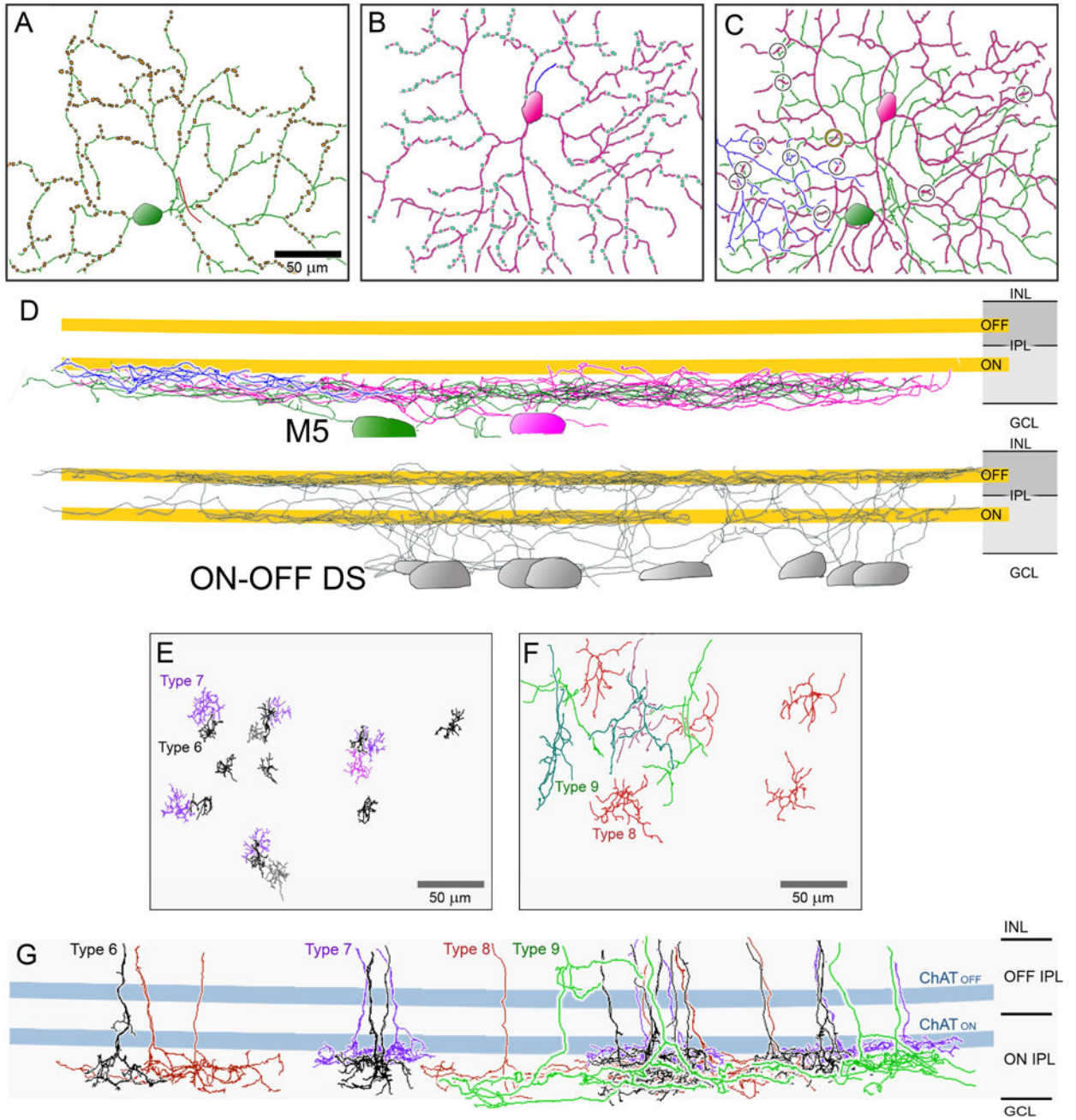
Fig. 4. Serial blockface electron-microscopic (SBEM) reconstruction of bipolar input to M5 ipRGCs

(**A–C**) Dendritic architecture of three presumptive M5 cells identified by reconstruction within a single small SBEM volume (Ding et al., 2016). Cell profiles are projected onto the retinal plane. Rectangular borders mark boundary of serial EM volume. Panels A and B show two cells in isolation (#7180 and #7027, respectively). Axons are indicated by contrasting color. Dots mark sites of ribbon synaptic contact onto the reconstructed cells. (**C**) Overlaid profiles of three M5 cells, including the two in panels A and B, and a third, incompletely reconstructed cell (blue) whose soma lies outside the volume. Circles mark sites of direct membrane contact between processes of two of the reconstructed ganglion

cells. (**D**) Projected side view of the same three cells. Dendritic stratification within the IPL is shown in relation to that of the ON and OFF ChAT bands (yellow) inferred from the stratification of 7 presumed ON-OFF DS cells (grey). (**E–G**). Architecture of cone bipolar cell Types 6 (grey/black), 7 (purple/pink), 8 (red), and 9 (green/blue) shown *en face* (**E–F**) and in side view (**G**). Slight variations in hues provide contrast for overlapping arbors. Scale bar = 50 μm.
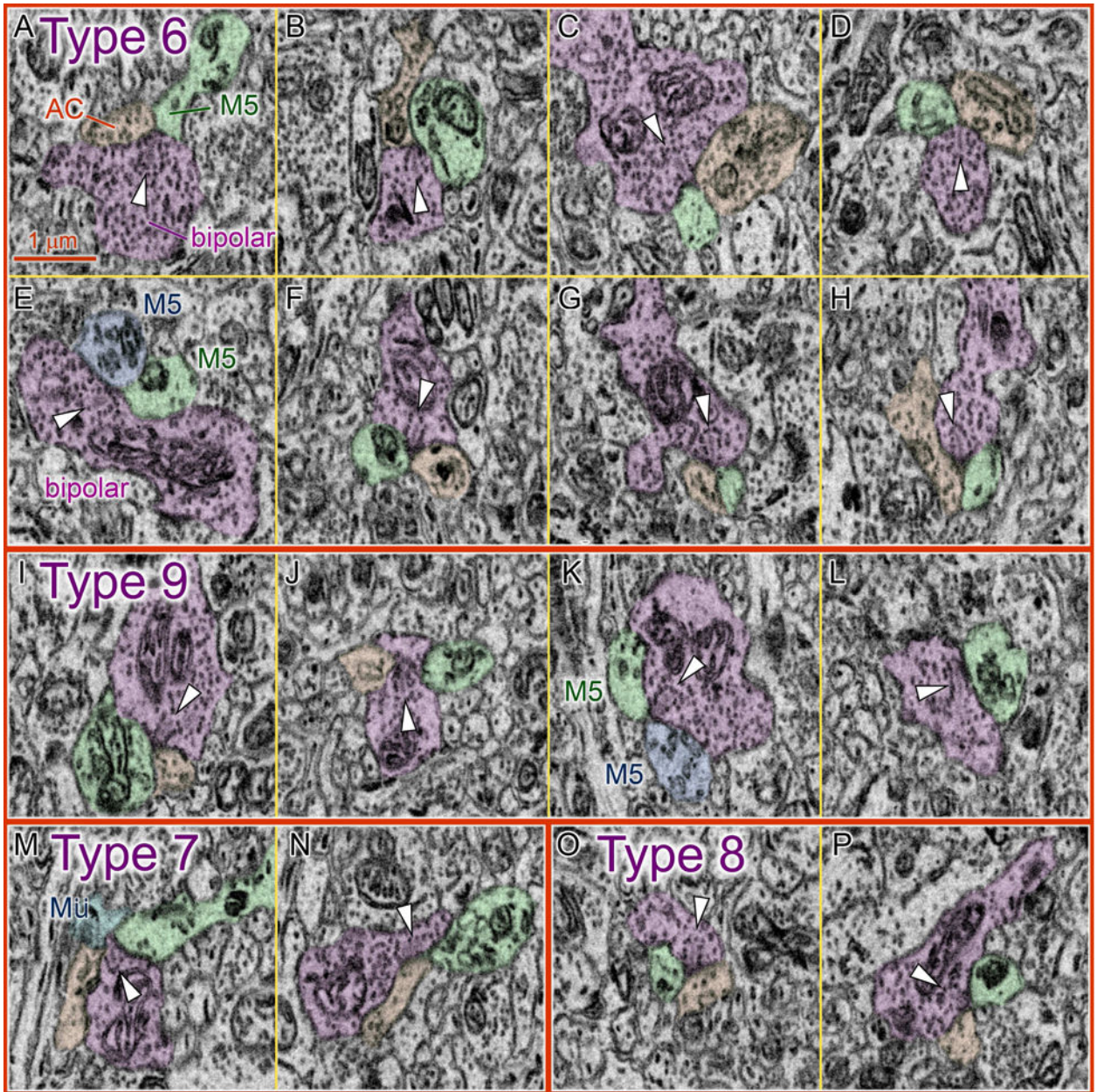
Fig. 5. Ultrastructure of bipolar ribbon synaptic contacts onto M5-cell dendrites

Serial blockface electron micrographs illustrating ribbon synaptic contacts between four types of ON cone bipolar axon terminals and postsynaptic dendrites of presumptive M5 ipRGCs from Fig. 4. Tints indicate identity of selected profiles. *Purple*: presynaptic bipolar-cell terminal; *green* (and blue in **E** and **K**): postsynaptic M5-cell dendrite; *orange*: postsynaptic amacrine-cell process. Arrowheads mark synaptic ribbons. Synaptic vesicles are darker than ribbons. Inputs from **A–H**: Type 6 ON cone bipolar cells; **I–L**: Type 9; **M–N**: Type 7; **O–P**: Type 8. In two cases (**E, K**), both postsynaptic processes at the dyad synapse were M5-cell dendrites. Ribbon synapse in L is a dyad, but the other postsynaptic partner is not visible in this plane. Blue profile in M is a Müller glial process ("Mü"), but

adjacent sections (not shown) indicate that the amacrine process (orange) is actually a postsynaptic target, with the M5 cell, at this dyad ribbon synapse. See also Movie File S1 and Table S1.
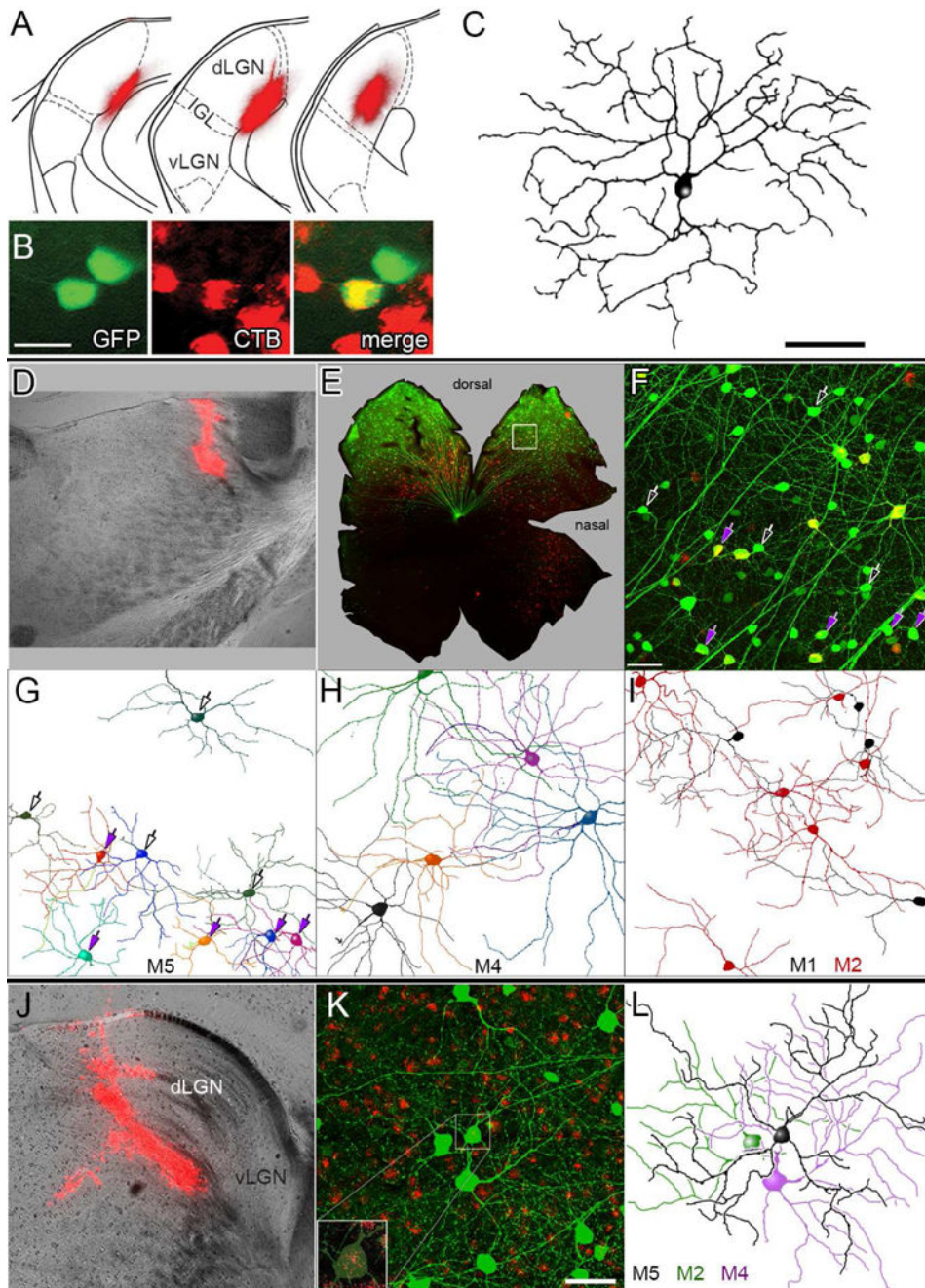
Fig. 6. Retrograde tracing shows M5 ipRGCs innervate the dLGN

(**A**) Retrograde tracer deposit in the left dLGN of an Opn4$^{Cre/+}$;Z/EG$^{+/−}$ mouse (cholera toxin β-subunit Alexa-594 conjugate). Fluorescence image (red) is superimposed on schematic dLGN coronal sections (adapted from Paxinos and Franklin, 2001; separated by 120 μm; left section most rostral). dLGN, vLGN: dorsal and ventral lateral geniculate nucleus; IGL = intergeniculate leaflet. (**B, C**) Retrograde labeling of an M5 ipRGC in the contralateral (right) retina (**A**). *Green*: melanopsin reporter (Cre-dependent GFP); *Red*: retrolabeling from dLGN. Scale bar = 20 μm. After intracellular dye-filling, the central, double-labeled ipRGC (yellow), showed characteristic M5 morphology, as documented in

the reconstruction in (**C**). Scale bar = 50 μm. (**D–I**) Morphology of ipRGCs retrolabeled by rhodamine beads deposited at the rostral pole of the dLGN. ipRGCs were identified profiles partially reconstructed, by virally induced Cre-dependent GFP labeling, induced in this Opn4$^{Cre/+}$ mouse by intraocular injection of an AAV2/2-CAG-FLEX-GFP virus and enhanced by anti-GFP immunofluorescence. (**E**) Low-magnification fluorescence photomontage of the flat-mounted left retina, contralateral to the deposit. *Red:* retrograde labeling; *green:* Cre-dependent viral GFP labeling; applies also to F. (**F**) Higher magnification view of region of interest (ROI) marked by the white box in E. Maximum-intensity projection of confocal optical sections spanning the inner plexiform and ganglion-cell layers. Purple arrows mark retrolabeled neurons presumed to be M5 cells, based on soma size and dendritic branching pattern and stratification (G). Other presumptive M5 cells lacking retrograde labeling are marked by hollow white arrows. Scale bar: 50 μm. (**G–I**) Somadendritic profiles of ipRGCs, sorted by presumed subtype and partially reconstructed from the ROI in F based on their Opn4-Cre-dependent viral labeling. Reconstructions are incomplete because only dendrites unambiguously traceable to the parent cell are included. (**G**) M5 cells; arrows (as in F) are purple for retrolabeled M5 cells. (**H**) M4 cells; all but the black cell are retrolabeled. (**I**) M1 and M2 cells. Four of six M2 cells are retrolabeled; among M1 cells, only that at lower left was retrolabeled. (**J–L**) Similar reconstruction of another presumed M5 cell, retrolabeled by the rhodamine bead injection into the dLGN shown in (J). (**K**) Maximum-intensity projection of Cre-dependent, GFP labeling of ipRGCs (green; enhanced by immunofluorescence) and retrograde labeling with rhodamine beads (red). Inset shows an enlarged view of the boxed M5 soma, with GFP signal dimmed to better reveal retrolabeling. (**L**) Partial reconstruction of somadendritic arbor of this retrolabeled presumptive M5 cell (black) and of two neighboring cells (M2 and M4; neither with clear retrolabeling). Scale bar: 50 μm.
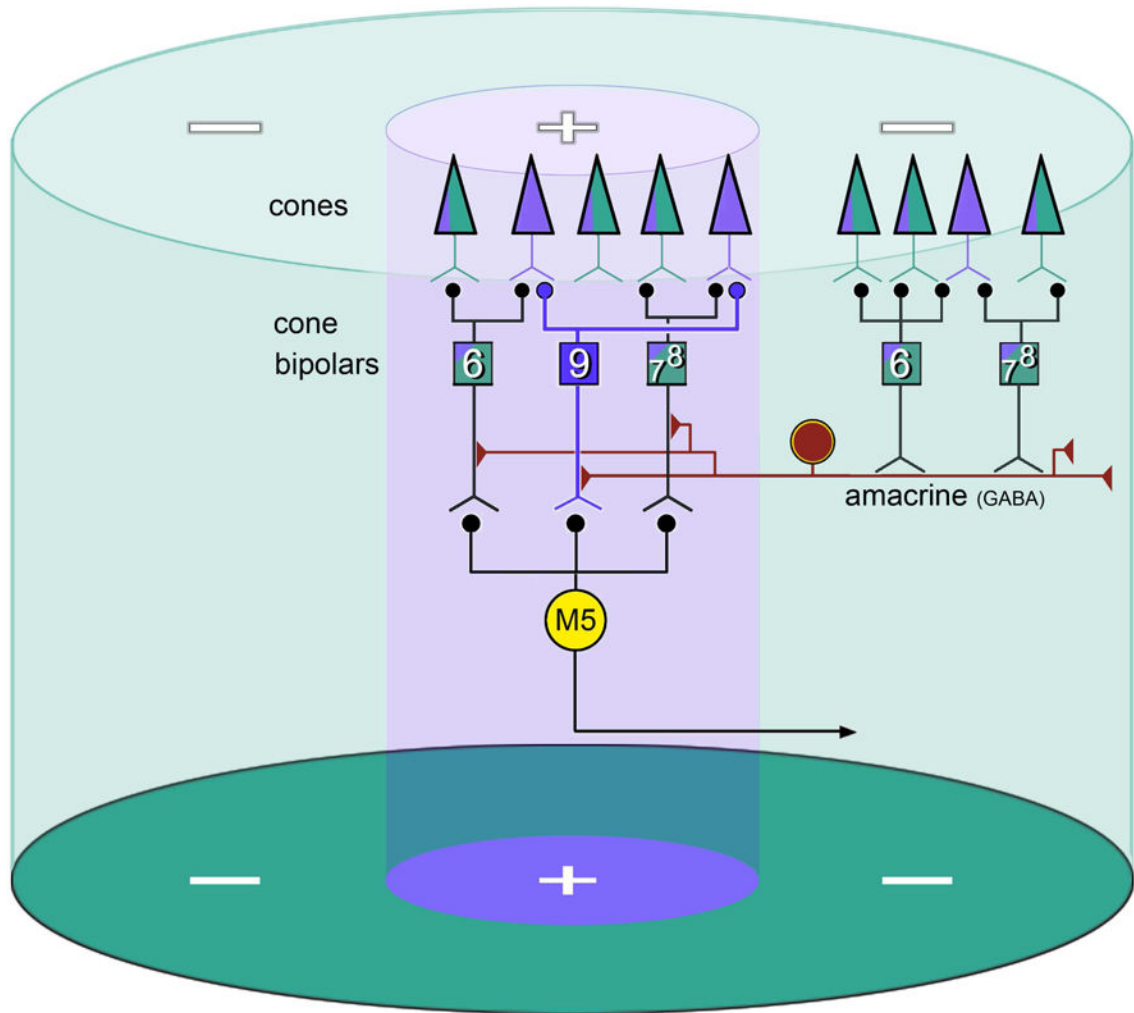
Fig. 7. Schematic summary of inferred synaptic circuitry underlying spatial segregation of cone inputs to M5 cells

Murine cone outer segments (triangles) contain either pure UV cone opsin (purple) or a mixture of UV and M-cone opsin (green). Bipolar cell Types 6–8 sample from all cone types whereas Type 9 bipolar cells sample selectively from cones containing only UV opsin. The M5 ipRGC (yellow circle) builds a receptive field center from inputs from Type 6-8, as well as Type 9 bipolar. Surround antagonism derives from wide-field spiking GABAergic amacrine cells that sample from bipolar Types 6–8 but not from Type 9, and are thus better activated by M than by UV cone-opsin drive.

Table 1

Group data on the morphology of three types of monostratified ON ipRGCs.

	M2 *n* = 20	M4 *n* = 27	M5 *n* = 44
Soma diameter (µm)	15.8 ± 1.7 [**]	21.1 ± 1.9 [***]	14.2 ± 2.4
Dendritic-field diameter (µm)	316.6 ± 61.9 [***]	359.6 ± 66.3 [***]	223.7 ± 43.9
Total dendritic length (µm)	2957 ± 733	4751 ± 1001 [***]	2851 ± 843
Total branch points	23.6 ± 6.8 [***]	38.2 ± 8.5 [***]	52.1 ± 12.5
# of primary dendrites	4.2 ± 1.2	5.3 ± 1.1 [***]	4.1 ± 1.3

Values listed are mean ± standard deviation. M2 and M4 values tabulated from Estevez et al., 2012 and compared to M5 cells. See also Fig. 1. Asterisks indicate statistically significant differences from values for M5 cells:

[**]
p < 0.01;

[***]
p < 0.001